Supporting Information

Rutile Alloys in the Mn-Sb-O System Stabilize Mn^{+3} to Enable Oxygen Evolution in Strong Acid

Lan Zhou[1], Aniketa Shinde[1], Joseph H. Montoya [2], Arunima Singh[3,4], Sheraz Gul[5], Junko Yano[3,5], Yifan Ye[3,4,6], Ethan J. Crumlin[6], Matthias H. Richter[1,7], Jason K. Cooper[3,4], Helge S. Stein[1], Joel A. Haber[1], Kristin A. Persson[2,3,8,], John M. Gregoire[1,*]*

[1] Joint Center for Artificial Photosynthesis, California Institute of Technology; Pasadena, CA 91125, USA.
[2] Environmental Energy Technologies Division, Lawrence Berkeley National Laboratory, Berkeley, CA 94720, USA.
[3] Joint Center for Artificial Photosynthesis, Lawrence Berkeley National Laboratory, Berkeley, CA 94720, USA.
[4] Chemical Sciences Division, Lawrence Berkeley National Laboratory, Berkeley, CA 94720, USA
[5] Molecular Biophysics and Integrated Bioimaging Division, Lawrence Berkeley National Laboratory, Berkeley, CA 94720, USA.
[6] Advanced Light Source, Lawrence Berkeley National Laboratory, One Cyclotron Road, Berkeley, California 94720, USA
[7] Division of Chemistry and Chemical Engineering, California Institute of Technology, Pasadena, CA 91125, USA
[8] Department of Materials Science and Engineering, University of California, Berkeley, CA 94720, USA.

*Correspondence to: Kristin A. Persson (kapersson@lbl.gov), John M. Gregoire (gregoire@caltech.edu)

Library synthesis

$Mn_xSb_{1-x}O_z$ composition libraries were synthesized using reactive RF magnetron co-sputtering of Sb and Mn metal targets onto different types of substrates (Si wafer with Pt conducting layer and Ti adhesion layer and glass substrates with Fluorine-doped SnO_2 (FTO) conducting layer. A summary of the libraries with deposition and thermal process conditions is provided in Table S1.

Table S1. Summary of Mn-Sb oxide composition libraries with synthesis conditions.

Library /film	**Substrate**	**O_2/Ar (mTorr/mTorr)**	**Annealing process (in air)**	**Sb power (W)**	**Mn power (W)**	**Figure(s) in main text**
A_700	Pt/Ti/SiO_2/Si	0.6/5.4	700 °C, 3 hrs	24	146	Fig.1a, 1d, 2a, 7, 8
A_550			550 °C, 10 hrs			Fig.1b
B_asdep	Pt/Ti/SiO_2/Si	1.2/4.8	NA, as-dep	46	150	Fig.1c, 1d
B_850			850°C, 3 hrs			N
C	Pt/Ti/SiO_2/Si	0.6/5.4	900°C, 3 hrs	30	150	N
D	FTO Tec7 glass	0.6/5.4	550 °C, 10 hrs	18	105	Fig.2b
E	FTO XG glass	0.6/5.4	700 °C, 3 hrs	42	142	N
F_700	Pt/Ti/SiO_2/Si	1.2/4.8	700 °C, 3 hrs	22	150	Fig.4
G_550	FTO Tec7 glass	0.6/5.4	550 °C, 10 hrs	20	100	Fig.3, 9

Combinatorial electrochemistry on Mn-Sb oxide composition libraries

- Libraries on glass substrates with FTO coating

Libraries (D and E) deposited on glass substrates with an FTO conducting layer were synthesized and characterized to confirm that the catalytic activity is not reliant on the underlying Pt layer, and while these experiments confirm the activity of the Sb-Mn oxides, those films are not amenable to further characterization due to interference from the SnO_2 in both XRD and XRF measurements. The catalytic stability of the most Mn-rich rutile sample in library D was evaluated by performing multiple CVs in 1.0 M H_2SO_4 solution between 1.24 and 1.79 V vs RHE at a scan rate of 0.02 V s^{-1}, see Figure 2b in the main text.

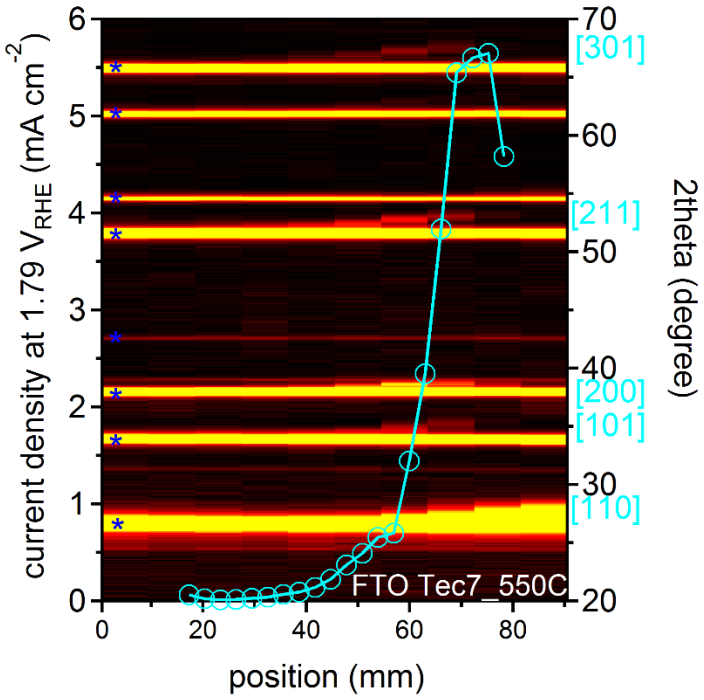

Figure S1. The current density obtained at 1.79 V vs RHE from CVs in 1.0 M H_2SO_4 (aq) on a series of $Mn_xSb_{1-x}O_z$ compositions from library D (deposited on FTO-coated Tec7 glass and subsequently annealed at 550 °C in air) is shown as a function of position along the composition gradient and is superimposed on the 2D XRD heatmap showing a series of 10 XRD patterns. FTO peaks are indicated with blue * and the rutile structure peaks are labelled in cyan on the XRD heatmap, revealing that the sharp increase in current density coincides with detection of the rutile alloy peaks.

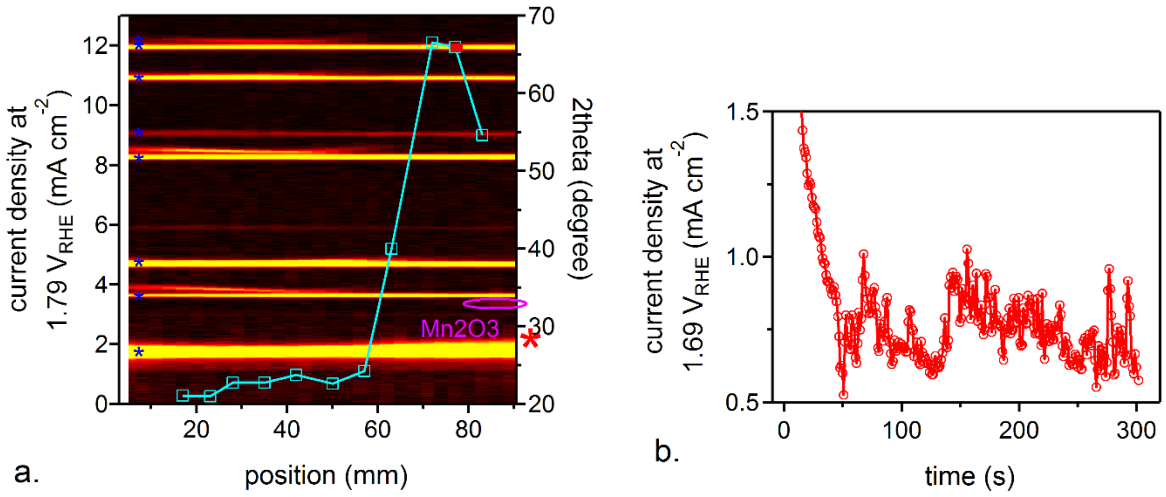

Figure S2. (a) Overlay of current density from CVs in 1.0 M H_2SO_4 (aq) and XRD heatmap (analogous to Figure S1) for a series of $Mn_xSb_{1-x}O_z$ compositions from Library E (deposited on FTO-coated XG glass and subsequently annealed at 700 °C in air). FTO peaks are indicated with blue * and the most Mn-rich rutile [110] peak is indicated with a red * in XRD heatmap. (b) 300 second CA measurement at 1.69 V vs RHE in the same electrolyte was performed on the high performance sample (most Mn-rich rutile sample, marked in red) at position 75 mm.

- Library A_700, A_550, and B_asdep on Pt/Ti/SiO_2/Si substrates

See main text Figure 1a, b, and c.

- Library B_850 deposited on Pt/Ti/SiO_2/Si substrate and annealed at 850 °C

XRD characterization of the library (B_850) annealed at 850 °C in Figure S3a reveals that the presence of the rutile structure across the entire composition range, including a phase mixture with the monoclinic and orthorhombic SbO_2 in Sb-rich region ($x<0.30$), a phase mixture with hexagonal $MnSb_2O_6$ for $0.30<x<0.57$, and a phase mixture with Mn_2O_3 for $x>0.57$. At $x<0.30$, the known tri-rutile structure $MnSb_2O_6$ is observed where the $(Mn,Sb)O_2$ rutile alloy exhibits longer range ordering that gives rise to the tri-rutile ordering peak near $2\theta = 19°$ and 21°. At higher Mn concentrations this ordering peak is not observed and the remaining diffraction peaks are indexed to a rutile alloy (ICDD 04-011-4962), where Mn and Sb are assumed to be randomly distributed on the cation sites. Similar to our observation from library (A_700) annealed at

700 °C, the transition from tri-rutile to rutile structure around x=0.30 is accompanied by a non-monotonic peak shifting as a function of composition and proceeds until the phase boundary near x = 0.57, where the rutile alloy coexists with Mn_2O_3. Moreover, annealing at the higher temperature of 850 °C, the transition from the tri-rutile to the rutile structure is also accompanied by formation of the polymorph hexagonal phase $MnSb_2O_6$ (ICDD 04-010-3922), see Figure S3b. The CV curve between 1.24 and 1.79 V vs RHE in Figure S3c indicates the relatively poor electrocatalytic activity of this hexagonal polymorph.

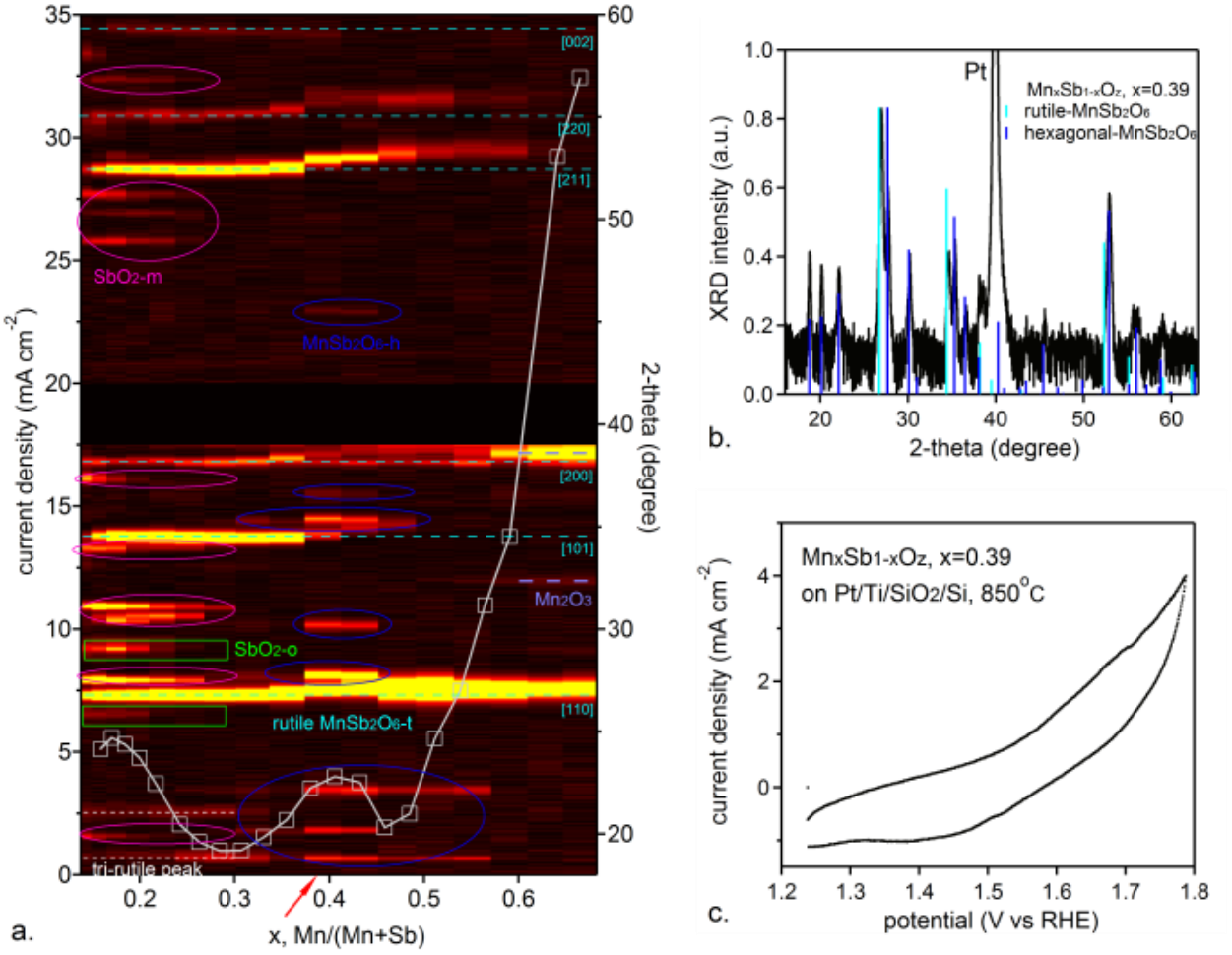

Figure S3. (a) 2D XRD plot of $Mn_xSb_{1-x}O_z$ compositions from Library B_850 (deposited on Pt/Ti/SiO_2/Si and subsequently annealed at 850 °C in air) with phases labelled in different colors. The current density obtained at 1.79 V vs RHE from each CV measurement in 1.0 M H_2SO_4 solution, as a function of x in $Mn_xSb_{1-x}O_z$, is superimposed on the 2D XRD heatmap. The red arrow around x = 0.39 indicates the sample where the most hexagonal $MnSb_2O_6$ phase mixed with rutile polymorph. The XRD and CV curve of this sample is shown in (b) and (c).

As noted above, the higher annealing temperature of 850 °C results in formation of a less catalytically active film containing the hexagonal $MnSb_2O_6$ phase. To assess any variation in phase behavior and catalytic activity with decreasing annealing temperature, Figure 1 in the main text shows the phase distributions of three $Mn_xSb_{1-x}O_z$ libraries annealed at 700 °C, 550 °C, and as-deposited. Note that we perform aggressive subtraction of slowly varying signals to facilitate visualization of weak XRD peaks, a data processing step that removes most signal from any amorphous material. As noted above, the phase boundary for the rutile alloy is near x = 0.30, but this data shows that in the lower-Sb, 2-phase region, the rutile structure is observed down to x = 0.1. With the lower 550 °C annealing, no crystalline signal is observed in this composition range and the rutile alloy is only obtained above x = 0.42. This trend of higher critical Mn concentration for rutile crystallization with decreasing temperature extends to the as-deposited library where weak rutile peaks are observed starting at x = 0.55. The lower crystallization temperature at higher Mn concentrations is counterintuitive given the higher above-hull ΔE_{form} (Figure 5 in the main text) and broader XRD peaks (Figure S10). This observation brings into question whether the peak broadening in this composition region is dictated by finite crystallite sizes, as the observation of variability in Mn oxidation state within a given alloy composition may give rise to a distribution of lattice parameters among the crystallites in a given composition sample. This motivates future characterization of the nanostructure of the Mn-rich rutile alloys to further understand their solid state chemistry and relationship to OER electrocatalysis.

Combinatorial electrochemistry on Library A_700: deposited on Pt/Ti/SiO_2/Si and annealed at 700 °C in air

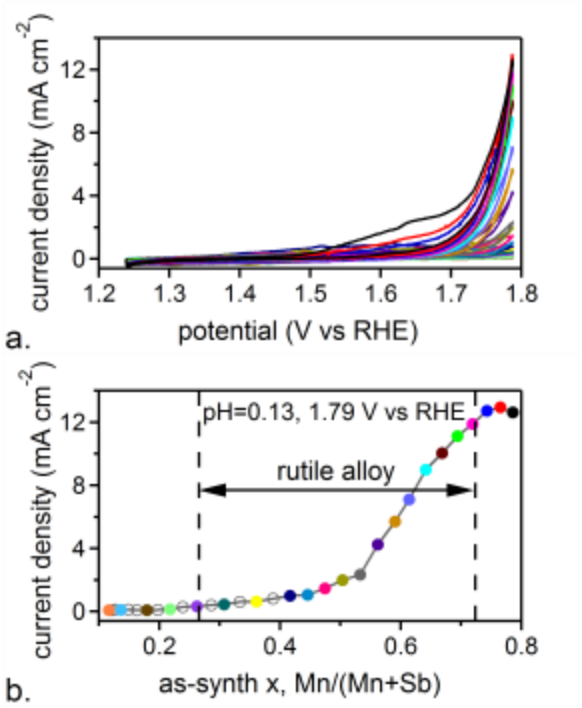

Figure S4. (a) Cyclic voltammograms (CVs, 0.02 V s^{-1}) acquired in 1.0 M H_2SO_4 (aq) solution on a series of $Mn_xSb_{1-x}O_z$ compositions (x = 0.11 to 0.78) deposited as a composition library on Pt/Ti/SiO_2/Si and subsequently annealed at 700 °C in air. (b) The current density obtained at 1.79 V vs RHE from each CV, as a function of x in $Mn_xSb_{1-x}O_z$. The data points are color-coordinated with the CVs shown in (a). The composition range observed to be phase-pure rutile is indicated.

Figure S4a shows a series of CVs obtained from the binary composition library annealed at 700 °C when the applied potential was scanned at 0.02 V s^{-1} in the range of 1.24 to 1.79 V vs RHE. The current density obtained at 1.79 V vs RHE plotted in Figure S4b indicates improved OER catalytic activity with increasing Mn concentration in the $Mn_xSb_{1-x}O_z$ composition library, with a particularly abrupt increase in electrocatalytic activity at x = 0.53. The data points are color-coordinated with the CVs shown in Figure S4a, and the overpotential to produce 10 mA cm^{-2} is approximately 548 - 558 mV for films with x = 0.67 - 0.78. While this overpotential is

higher than those reported for IrO_2 and RuO_2,[1] it is among the best reported for non-precious-metal catalysts in strong acid.

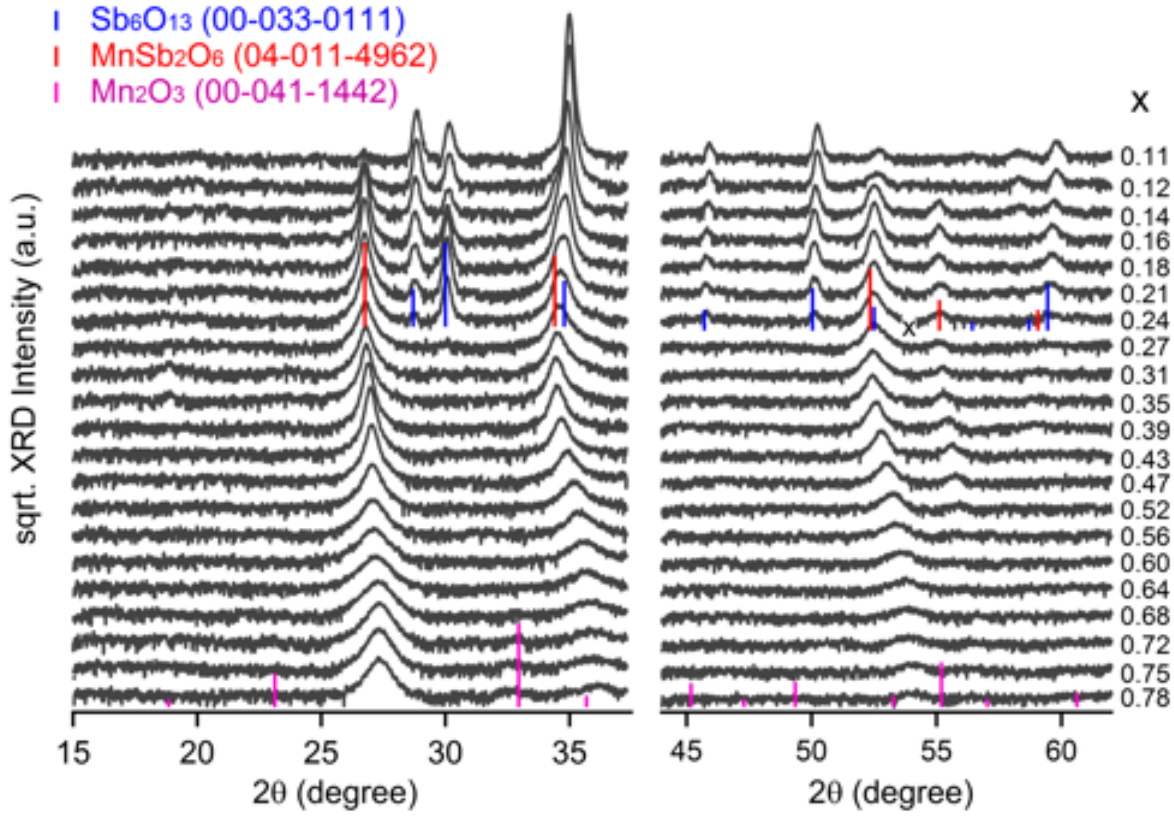

Figure S5. XRD patterns of $Mn_xSb_{1-x}O_z$ binary composition spread annealed at 700°C (library A_700) with Mn concentration x from 0.11 to 0.78.

XRD characterization of the as-synthesized $Mn_xSb_{1-x}O_z$ library annealed at 700 °C is summarized in Figure S5 and reveals the presence of a rutile structure across the entire composition range, including a phase mixture with the Sb_6O_{13} structure for $x < 0.27$ and a phase mixture with the Mn_2O_3 structure for $x > 0.70$, which are the boundaries of the phase-pure rutile alloy shown in Figure S4b. To further elucidate the phase-dependent electrochemistry, XRF measurements were performed before and after the CVs in Figure S4 to assess corrosion of both Sb and Mn during the CV (Figure S6). Sb loss was only observed in the most Sb-rich compositions containing the Sb_6O_{13} structure, suggesting electrochemical instability of Sb in this phase, which also did not exhibit substantial catalytic activity. Mn corrosion is evident for all

Mn-rich (x > 0.50) compositions with a sharp increase in corrosion where the Mn_2O_3 structure is observed (x > 0.70). Inspection of the anodic sweeps in Figure S4a reveals that only these Mn_2O_3-containing compositions exhibit substantial oxidative current above the catalytic current, assuming that the OER current increases approximately exponentially with increasing potential. The absence of a similar cathodic wave on the cathodic sweep indicates that this non-catalytic oxidation process is not reversible, suggesting that in this potential range Mn corrodes from the Mn_2O_3 structure. These results demonstrate that the best catalysis that is stable on the time scale of the measurements occurs in the most Mn-rich films where only the rutile phase is observed, prompting further analysis of $(Sb,Mn)O_2$ rutile alloys.

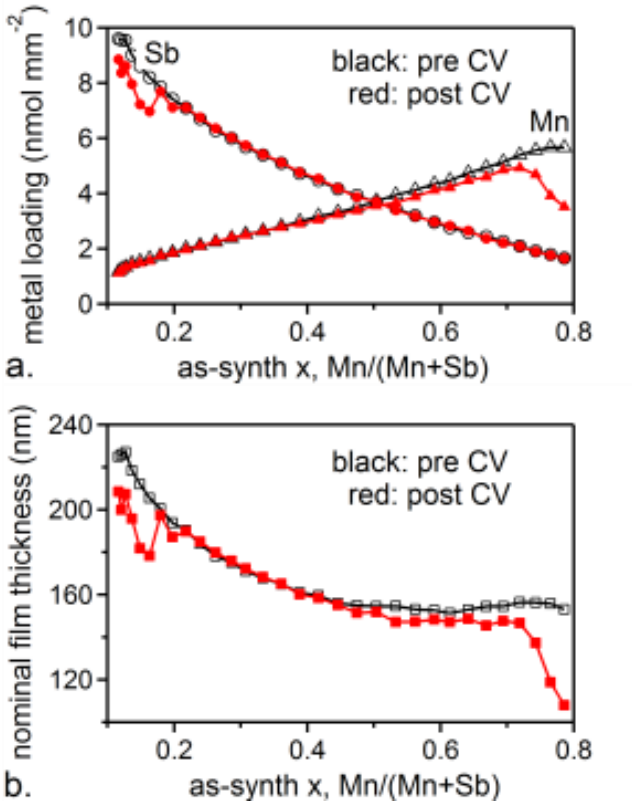

Figure S6. (a) The metal loading and (b) nominal film thickness derived from XRF measurements, assuming the bulk density of rutile $MnSb_2O_6$, before and after one CV cycle (Figure S4a), as a function of Mn concentration in the $Mn_xSb_{1-x}O_z$ composition library annealed at 700 °C (library A_700).

Given the unprecedented discovery of catalytic activity with non-precious metal oxides at low overpotential, a potential of 1.69 V vs RHE (460 mV overpotential) was chosen for further characterization of catalyst performance via 200 s CA measurements of the phase-pure rutile portion of the composition library as well as the x = 0.72 sample where some Mn_2O_3 is present. The CA data is shown in Figure S7 and the current density at the end of each CA is shown in Figure 2a, which confirms the observation from Figure S4 that the Mn-rich alloys provide the highest catalytic activity. XRF characterization reveals that Mn corrosion also increases with as-synthesized Mn concentration (Figure S8a), and in particular the Mn-rich samples with as-synthesized x = 0.64 and 0.72 both corroded to x = 0.58 during the 200 s measurement. The x = 0.64 sample exhibited the highest current density just above 1 mA cm^{-2} at the end of the 200 s measurement, and the ensuing CV of this sample (Figure S8b) demonstrates that the excellent catalytic activity is maintained even after the loss of approximately 10% of the Mn in the film. The overpotential to produce a current density of 10 mA cm^{-2}, averaged over the anodic and cathodic sweeps to mitigate influence of capacitive current, is 515 mV.

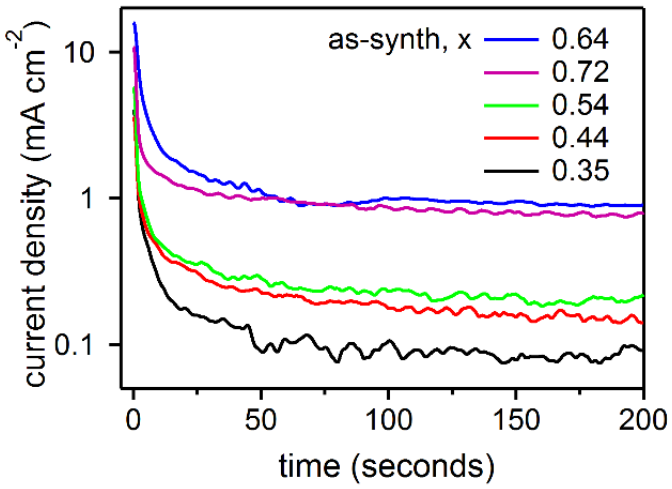

Figure S7. 200 second CA measurements at 1.69 V vs RHE in 1.0 M H_2SO_4 solution of the phase-pure rutile portion of the $Mn_xSb_{1-x}O_z$ composition library (library A_700) as well as the x = 0.72 sample where some Mn_2O_3 is present.

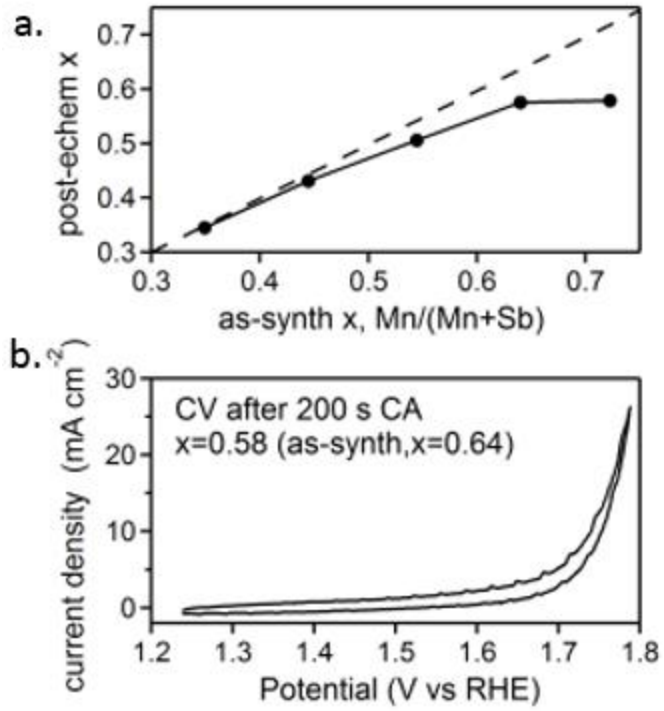

Figure S8. (a) The XRF-determined composition change after 200 s CA measurement at 1.69 V vs RHE in 1.0 M H_2SO_4 aqueous solution. The sample with highest current density at the end of the 200 s CA measurement had an as-synthesized Mn concentration of x = 0.64 that decreased to 0.58 during the CA. (b) The CV curve of this sample after the post-CA XRF measurement, demonstrating excellent activity despite previous Mn loss.

The stoichiometric phase $MnSb_2O_6$, corresponding to the x = 0.33 sample in this work, was recently reported as an OER catalyst in 1.0 M H_2SO_4 electrolyte and 60% Mn loss was observed over 168 hours of operation.[2] These results are in reasonable agreement with Figures S4 where the compositions near x = 0.33 have little catalytic activity below 500 mV overpotential and also exhibit little Mn loss during the 200 s CA. The x = 0.64 sample is still observed to be in the rutile crystal structure after the CA and CV measurement of Figure S8 (Figure S9). This compendium of results raises a suite of questions regarding the materials chemistry of Mn-rich Mn-Sb rutile alloys, which we address in the following sections to provide additional understanding of this new class of OER electrocatalysts.

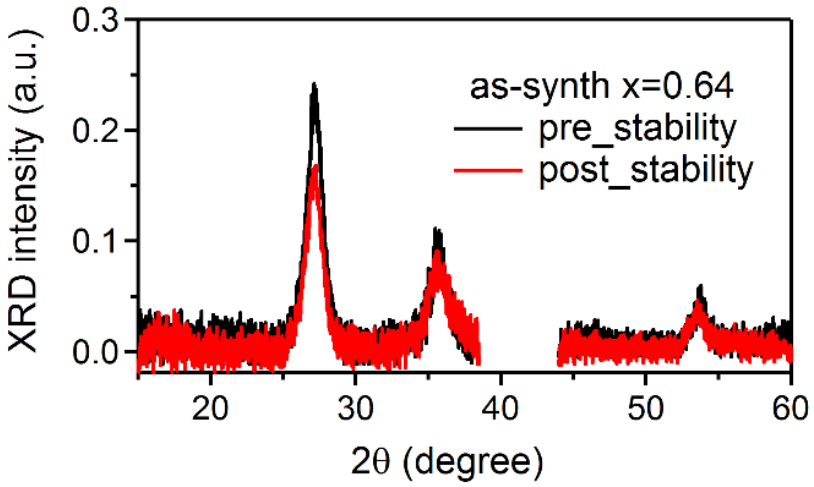

Figure S9. XRD patterns of as-synthesized (black, "pre_stability") and post-electroechemistry (red, "post_stability") of $Mn_xSb_{1-x}O_z$ sample with as-synthesized Mn concentration of 0.64 (library A_700). The strong signal from Pt layer is omitted for clarity. There is no change in the rutile structure after 200 s CA at 1.69 V vs RHE and 1 cycle of post-CA CV scan (1.24 to 1.79 V vs RHE, 0.02 V s^{-1}) in 1.0 M H_2SO_4 aqueous solution. However, the post-echem XRD shows decrease in signal intensity due to the materials corroding away during the electrochemistry as indicated by the composition change observed from XRF measurements (Figure S8a).

Phase behavior of Library A_700: deposited on Pt/Ti/SiO_2/Si and annealed at 700 °C in air

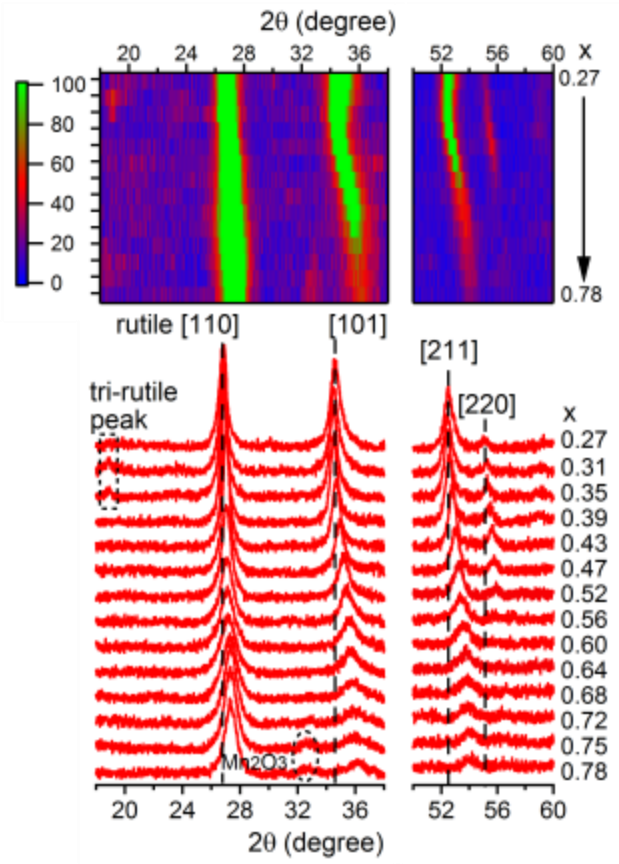

Figure S10. XRD patterns of $Mn_xSb_{1-x}O_z$ binary composition library annealed at 700 °C with Mn concentration x = 0.27 - 0.78. Each horizontal slice in the upper 2D plot corresponds to one XRD curve in the stacked 1D plot below. The intense diffraction peaks from the Pt substrate were omitted for clarity.

Figure S10 summarizes XRD analysis of the x = 0.27 to 0.78 portion of the $Mn_xSb_{1-x}O_z$ composition library annealed at 700 °C in air. At x = 0.27, 0.31 and 0.35, the known tri-rutile structure (space group $P4_2/mnm$) $MnSb_2O_6$ is observed where the $(Mn,Sb)O_2$ rutile alloy exhibits longer range ordering that gives rise to the tri-rutile ordering peak near 2θ = 19°. At higher Mn concentrations, this ordering peak is not observed and the remaining diffraction peaks are indexed to a rutile alloy (ICDD 04-011-4962) where Mn and Sb are assumed to be randomly distributed on the cation sites. The transition from tri-rutile to rutile structure is accompanied by

a non-monotonic peak shifting as a function of composition that is discussed further below and proceeds until the phase boundary near x = 0.70. The nominal crystallite size of $MnSb_2O_6$ phase (calculated by the Scherrer formula using the [110] diffraction peak at 26.75°, see Figure S11) is approximately 20 nm with grain size decreasing as Mn concentration increases. Previous studies of the phase behavior of Mn-Sb oxides revealed alloying within the rutile structure up to x = 0.50,[3] and our observation of continued alloying up to x = 0.70 constitutes the discovery of new phase behavior in this system.

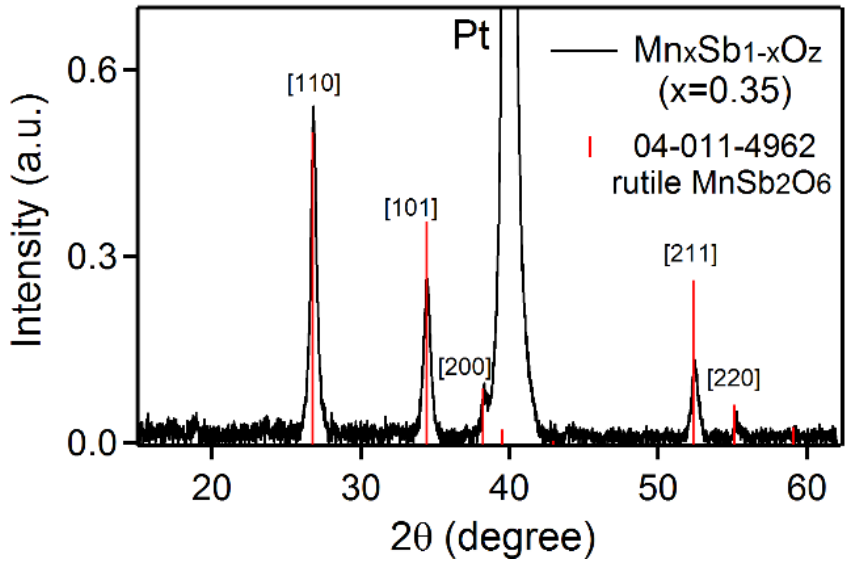

Figure S11. XRD pattern for the $Mn_xSb_{1-x}O_z$ sample in library A_700 with x = 0.35 along with the ICDD stick pattern of rutile structure $MnSb_2O_6$ (04-011-4962) and strong diffraction peak from the substrate Pt conducting layer. The grain size is approximately 20 nm calculated using the [110] diffraction peak at 2θ=26.75°.

X-ray Absorption Data collection and analysis on Library A_700:

X-ray absorption spectroscopy (XAS) measurements were performed at the Stanford synchrotron radiation light source on beamline 7-3 with the standard storage ring conditions of 3.0 GeV electron energy and 500 mA average current. The incident x-rays were monochromatized using a Si (220) double crystal monochromator which was detuned to 50% of flux maximum at the Mn/Sb

K-edge to minimize the higher harmonics. The intensity of the incident and transmitted x-rays was monitored using N_2 and Ar filled ion chambers (I_0, in front of the sample and I_1/I_2 after the sample) for Mn and Sb measurements, respectively. The sample spectra were collected in fluorescence mode using a 30-element Ge detector (Canberra). Monochromator energy was calibrated for Mn with $KMnO_4$ spectrum by assigning 6543.3 eV to the pre-edge peak, whereas for Sb the energy calibration was done using Sb foil spectrum by setting the first inflection point at 30491.0 eV. The individual Mn XAS spectra of samples were calibrated using a glitch in the I_0 intensity and Sb XAS spectra were calibrated by recording Sb foil (placed between I_1 and I_2 ion chambers) spectrum concomitantly with the sample measurements. The data for reference compounds were recorded in transmission mode after dilution with boron nitride (~1% w/w).

The XAS data reduction was carried out with the SamView program included in SixPack software package (http://www.sams-xrays.com/sixpack). Athena software, Demeter version 0.9.26,[4] was used for data averaging and removal of the pre-edge and post-edge background. To determine the average Mn oxidation state, linear combinations with a database of pure-valence species (the Combo method) were used.[5] In addition to the oxides spectra collected along with the samples, the database from Manceau *et. al.*[5] was also used after cross-calibrating by aligning Mn_2O_3 spectra in both data sets. Fitting was performed in the energy range 6535 - 6570 eV over the first derivatives of x-ray absorption near-edge structure (XANES) spectra in order to avoid errors originating from differences in post-edge normalization. In this method, data is fit to a linear combination of reference spectra with progressively removing the references with negative fractions. This empirical method provides a valence estimation with an accuracy of 0.04 valance units (v.u.) when the Mn^{2+} fraction is below 0.15. The accuracy decreases with increase in Mn^{2+} content but has been reported to be in the range 0.04-0.08 v.u.

For x-ray absorption fine structure (EXAFS) data a five-domain cubic spline was used to remove low-frequency background in *k*-space and resulting *k*-space data, as $k^3\chi(k)$, was then Fourier transformed into *r*-space over a *k* range of 2.6 to 11.4 $Å^{-1}$. EXAFS fitting was carried out using Artemis (Demeter software version 0.9.26) with phase and amplitude functions obtained from FEFF, version 6.[6] First shell fits were carried for the data corresponding to samples at two extremes in XAS data (x=0.35 and x=0.72) and best fit parameters are listed in Table S2. The variable parameters used include R (average bond distance between Mn and scattering atom) and σ^2 (mean

square displacement of the bond distance). The value of E_0 (the energy which corresponds to the zero value of the photoelectron wave vector k) was also included as a fit parameter. The value for S_0^2 (the amplitude reduction factor) was extracted from the fit to the data of $KMnO_4$, and was fixed (0.80) during the fits. The value of N (the number of atoms in the shell) was fixed to 6 in both samples. Only one Mn-O path was used in case of the sample with x = 0.35, providing a good fit as shown in Figure S12. For the x = 0.72 sample, the analogous fit poorly reconstructed the data, prompting variations of the fit to include a single additional fit parameter. Using N as a fit parameter with a single Mn-O distance resulted in N=4.3±0.2, but this corresponds to >20% oxygen vacancy concentration which we believe to be incorrect due to the high above-hull energy of oxygen vacancies. An additional 3 fit models were used, each using 2 Mn-O bond distance parameters with their respective bond counts set to (5, 1), (4, 2), and (3,3). The (4, 2) fit was reasonable with bond distances of 1.90±0.01 and 2.11±0.03, respectively. The (5, 1) fit was even better (Figure S12) with very similar bond distances shown in Table S2. The use of 1 bond distance for the Sb-rich composition and 2 bond distances for the Mn-rich composition is consistent with expectations from the observed primary oxidation states of Mn^{+2} and Mn^{+3}, respectively, the latter of which is known to exhibit large Jahn-Teller distortions.

Table S2: Best fit parameters corresponding to the first shells of samples at two extremes of rutile structure.[a]

Sample	Path	R (Å)	N	σ^2 (10^{-3} Å^2)	R-factor (%)	ΔE_0 (eV)
as-synth x = 0.35	Mn-O	2.13±0.01	6	7.61±0.88	1.10	0.23±1.25
as-synth x = 0.72	Mn-O	1.92±0.01	5	6.52±0.49	0.10	-4.33±0.63
	Mn-O	2.23±0.05	1	14.9±7.60		

[a]Fitting for sample x = 0.35 was performed over the *r*-range 1.0 ≤ R'(Å) ≥ 2.1 (*k*-range 2.51≤ k(Å^{-1}) ≥ 11.23). For EXAFS curve of sample x=0.72, data was fit for the *r*-range 1.0 ≤ R'(Å) ≥ 2.0 (*k*-range 2.75≤ k(Å^{-1}) ≥ 11.49).

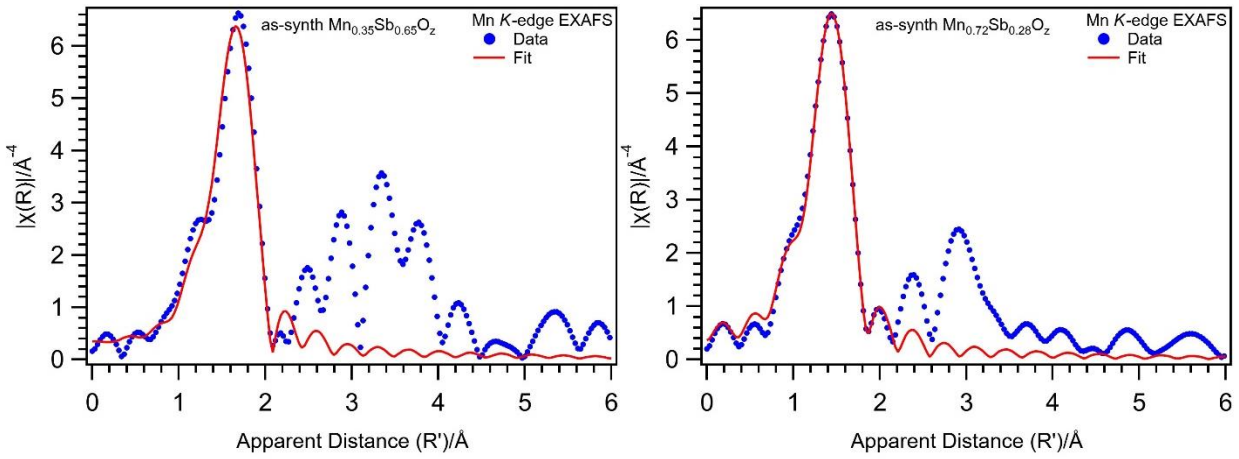

Figure S12. First shell fitting of EXAFS spectra from approximately the lowest and highest Mn concentrations in the rutile phase. See Table S2 for fitting details.

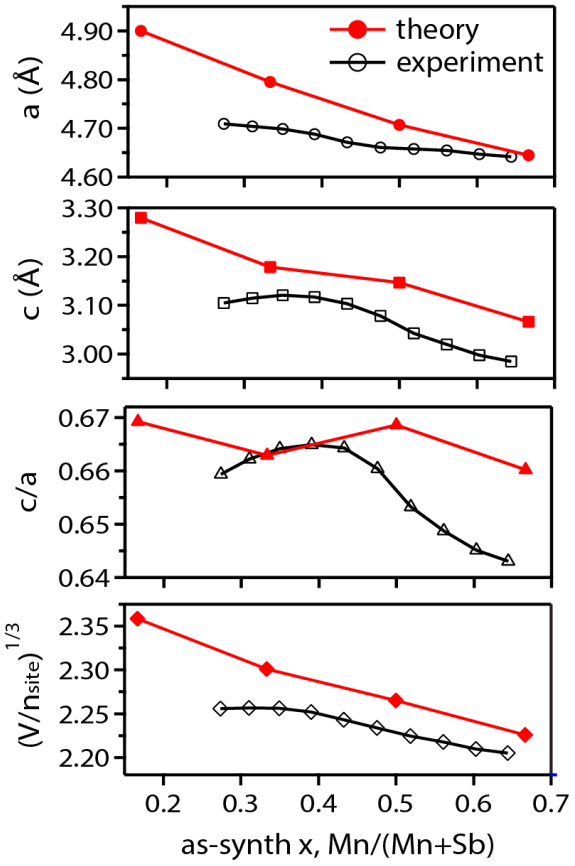

Figure S13. The lattice parameters of rutile crystal structure of a-axis, c-axis, ratio of c and a, cubed root of unit cell volume normalized by number of sites, both derived from x-ray diffraction data (black) and independently calculated via DFT (red), as a function of x in $Mn_xSb_{1-x}O_z$.

We return to the observation from Figure S10 that the positions of the XRD peaks shift non-monotonically as a function of alloy composition, corresponding to the lattice constant variation shown in Figure S13, which additionally contains the equivalent data for the series of calculated rutile alloys. A theory-experiment comparison reveals excellent qualitative and reasonable quantitative agreement, with perhaps the most salient features being (i) the systematic decrease in lattice volume with increasing Mn concentration and (ii) the highly nonlinear variation of the c/a aspect ratio. These observations may be explored in future work to gauge the influence of these structural variations on reactivity with the precursors and intermediates of the OER. [3a]

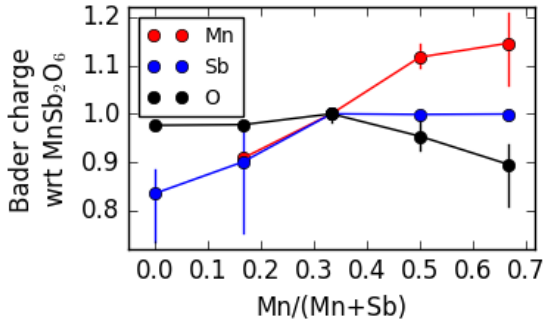

Figure S14. The Bader charge analysis of the 6 Mn and Sb cations and the 12 O anions in the alloy supercells are shown with respect to their values at the $MnSb_2O_6$ composition, with each vertical line and point representing the total spread of values within the supercell and the average values, respectively.

To further probe the underpinnings of increased Mn oxidation state with Mn concentration, we apply Bader charge analysis to the alloy models described above. Bader charge analysis has been shown to yield smaller absolute values of oxidation states than those of traditional construction of formal integer valences, prompting our semi-quantitative analysis of the Bader charge trends in Figure S14. The Sb and Mn Bader charges are scaled by the values for $MnSb_2O_6$, and the variation in Bader charge among the 6 cations, which are either Mn or Sb at a ratio corresponding to the composition x, is shown with vertical lines that span the minimum to maximum value. For the 2 most Sb-rich alloy compositions, which have not been experimentally observed, the Bader charge on the Sb cations exhibits considerable variability both within a

given supercell and as a function of x. At the $MnSb_2O_6$ and more Mn-rich compositions, the Sb Bader charge is constant, both with respect to alloy concentration and among the Sb sites in the supercell, which is in excellent agreement with the XAS results that the Sb K-edge does not change over this range of alloy compositions. The Bader charge on Mn sites increases with composition, in agreement with the XAS results, and at the 2 most Mn-rich alloys, the Mn sites in the supercell exhibit a substantial spread of Bader charge values, demonstrating variability in the Mn oxidation state in these rutile alloys, which may be particularly pertinent to the stabilization of surface Mn under OER operation as well as the OER catalytic activity. For these Mn-rich rutile alloys, given the slight increase in XAS-determined average Mn oxidation state after OER electrocatalysis, partial corrosion of Mn, and variation in Mn oxidation state within a given alloy composition, it appears that the lower-valent, near-surface Mn atoms are preferentially etched from the catalyst. The resulting hypothesis for the improved performance of the rutile alloys with increasing Mn concentration is that the stable, OER active sites are surface Mn with oxidation state near +3, whose concentration is enhanced with increased Mn alloying within the rutile structure and whose stability (compared to Mn oxides) is provided by surrounding Sb in the rutile alloy.

Information on other H-cell measurements

1. epoxy-encapsulated rutile electrode on FTO substrate (G_550, x = 0.70)

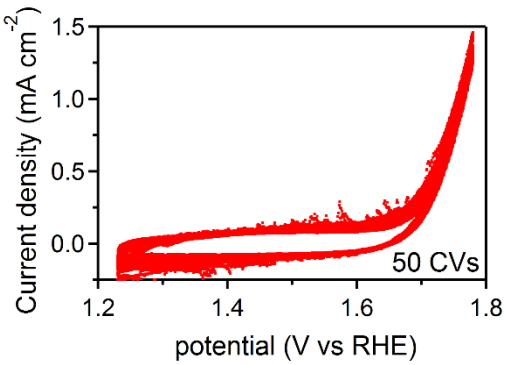

Figure S15. 50 CV sweeps between 1.23 and 1.78 V vs RHE of $Mn_{0.70}Sb_{0.30}O_z$ sample in 1 M H_2SO_4 solution and followed by UHV- and AP-XPS measurements.

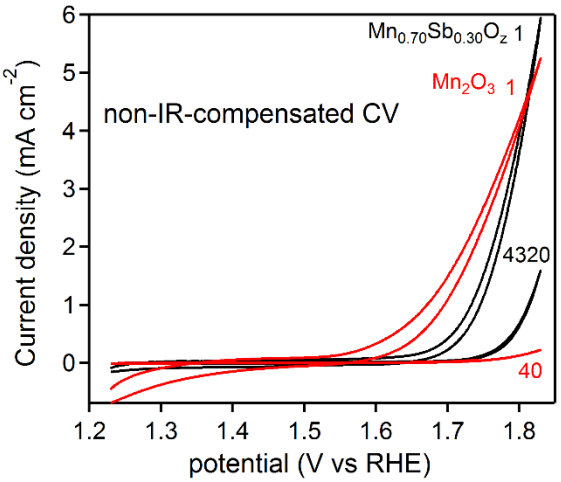

Figure S16. Non-IR compensated CV curves of epoxy-encapsulated rutile $Mn_{0.70}Sb_{0.30}O_z$ and Mn_2O_3 electrodes between 1.23 and 1.83 V vs RHE in 1.0 M H_2SO_4 electrolyte. The IR-corrected CVs are shown in Figure 3a.

2. epoxy-encapsulated rutile electrode on Pt/Ti/SiO_2/Si substrate (F_700, x = 0.67)

Electrochemical impedance spectroscopy (EIS) was performed on epoxy-encapsulated rutile electrode (0.22 cm^2) at 1.725 V vs RHE from 1 Hz to 300 kHz prior to the long CA in Figure 4a. The EIS model was fit using Gamry Echem Analyst software. The Equivalent Circuit used is a Randles circuit and yields the uncompensated resistance of 3.3 Ω. Fitting the model to a constant phase Randles-like circuit yields about the same result for the uncompensated resistance.

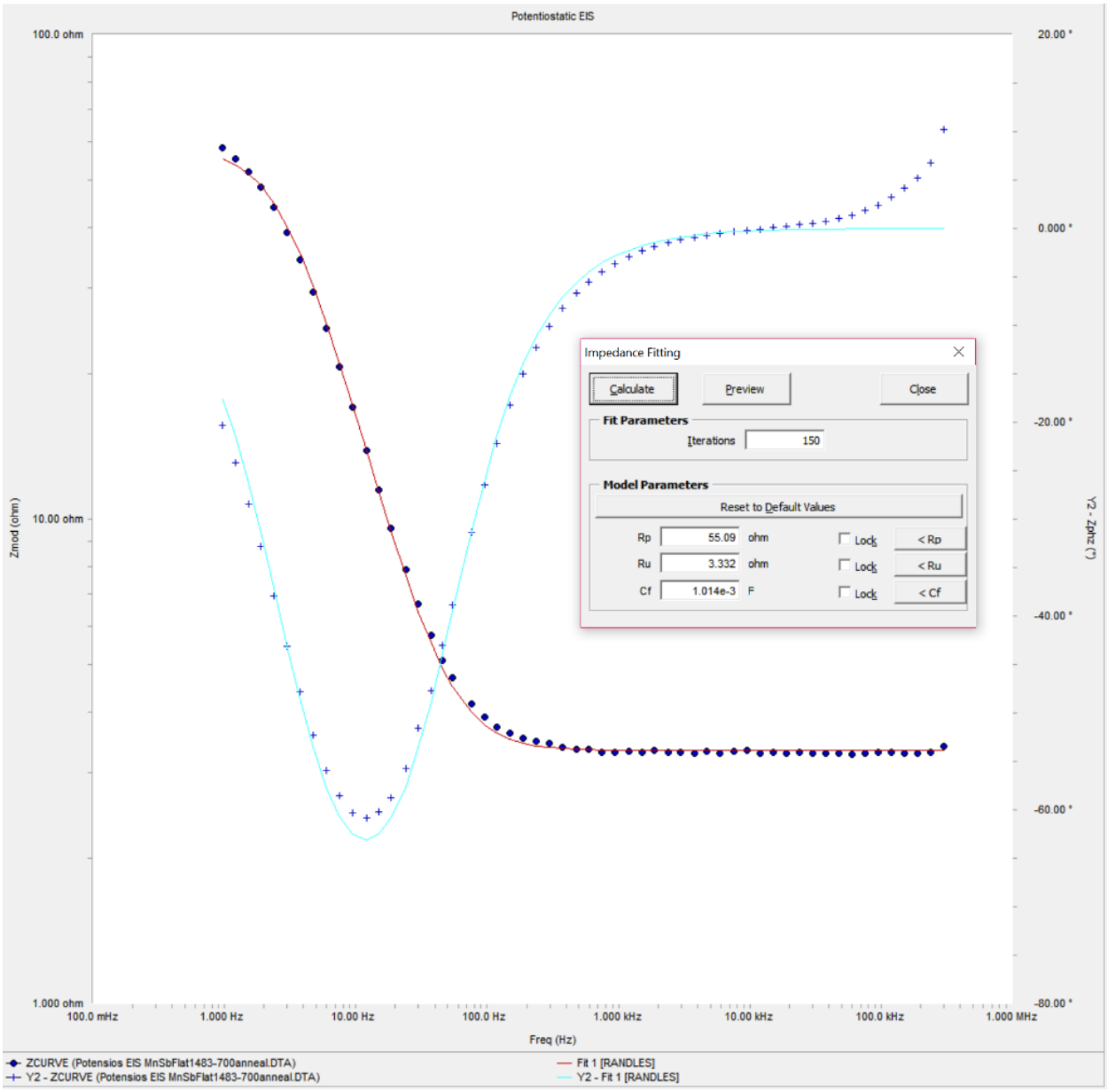

Figure S17. EIS Bode Plot fit to a Randles equivalent circuit.

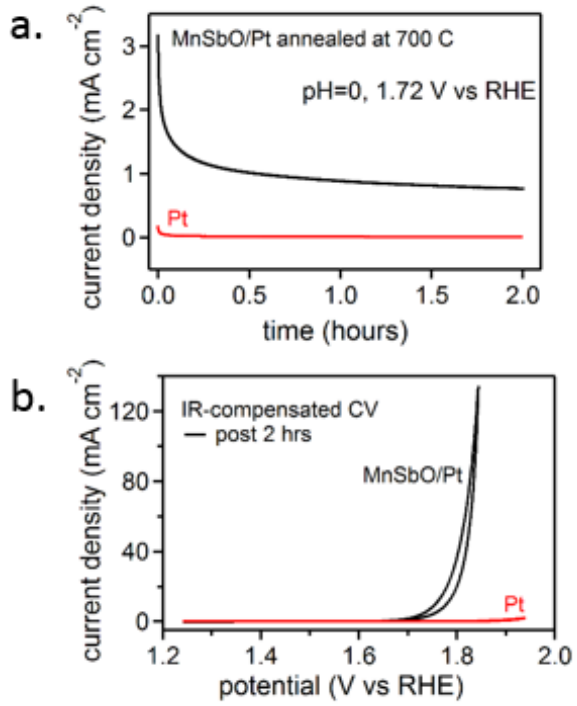

Figure S18. (a) 2 hours of CA measurements at 1.72 V vs RHE (490 mV overpotential) in 1.0 M H_2SO_4 solution of epoxy-encapsulated rutile $Mn_{0.67}Sb_{0.33}O_z$ electrode and Pt/Ti/SiO_2/Si substrate electrode, and (b) corresponding IR-compensated CVs at 0.01 V s^{-1} after CA. These measurements determine that the Pt conducting underlayer provides no meaningful contribution to the electrochemical characterization.

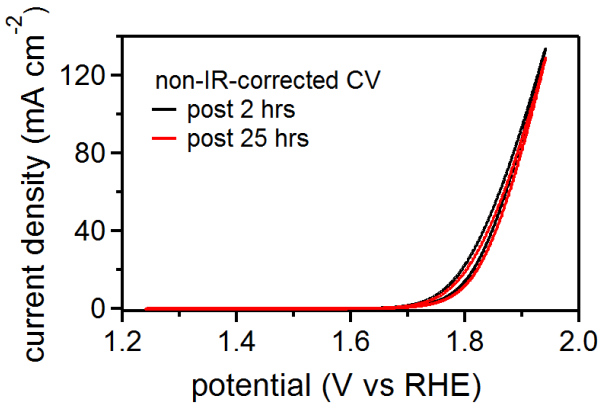

Figure S19: Non-IR corrected CV curves of epoxy-encapsulated rutile $Mn_xSb_{1-x}O_z$ electrode (x = 0.67) between 1.24 and 1.94 V vs RHE in 1.0 M H_2SO_4 electrolyte. The IR-corrected CVs are shown in Figure 4b. The uncompensated resistance value of our electrochemical cell is 3.3 Ω as determined by EIS measurement in Figure S17.

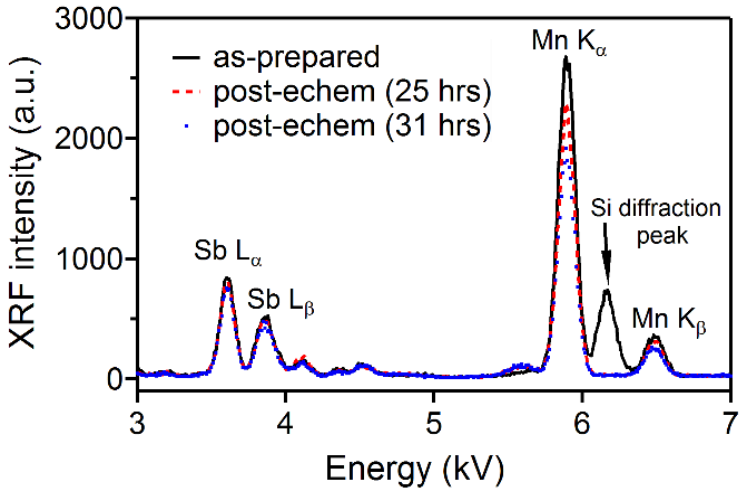

Figure S20. XRF spectra of epoxy-encapsulated rutile $Mn_xSb_{1-x}O_z$ electrode (x = 0.67) as-synthesized (annealed at 700 °C, black), post 25 hours (red), and 31 hours (blue) of electrochemistry.

Table S3. Bulk dissolution of Sb and Mn during the electrochemical operations (Figure 4) of epoxy-encapsulated rutile $Mn_xSb_{1-x}O_z$ electrode (x = 0.67) determined by XRF spectra shown in Figure S20.

	SbL	**MnK**	**Sb (nmol)**	**Mn (nmol)**	**Mn at.%**	**Sb+Mn loading (nmol mm^{-2})**
as_prepared	385.79	1544.32	21.18	43.09	67.04	20.47
post_echem_1 (~25 hrs)	375.97	1321.65	20.64	36.87	64.11	18.32
post_echem_2 (~30 hrs)	371.08	1152.53	20.37	32.16	61.22	16.73
Total loss			3.8%	25.4%	8.7%	18.3%

In order to determine the amount of Mn and Sb dissolution in electrolyte during H-cell measurements, 2.5 mL aliquots of sulfuric acid were taken from the working chamber and counter chamber and mixed with 2% nitric acid at various time points during electrochemical measurements. The resulting 5 mL samples were measured via ICP-MS and tested for presence of Mn, Sb, and precious metals, producing the results of Figure 3c and demonstrating the absence of precious metals. After the electrochemistry experiments, the carbon rod counter electrode was soaked in 10% nitric acid overnight and no Mn, Sb, or precious metals were found in ICP-MS analysis of the resulting solutions. Similarly no precious metals were found by ICP-MS after digesting the electrode of Figure 3 by soaking it overnight in 25% nitric acid.

DFT calculation

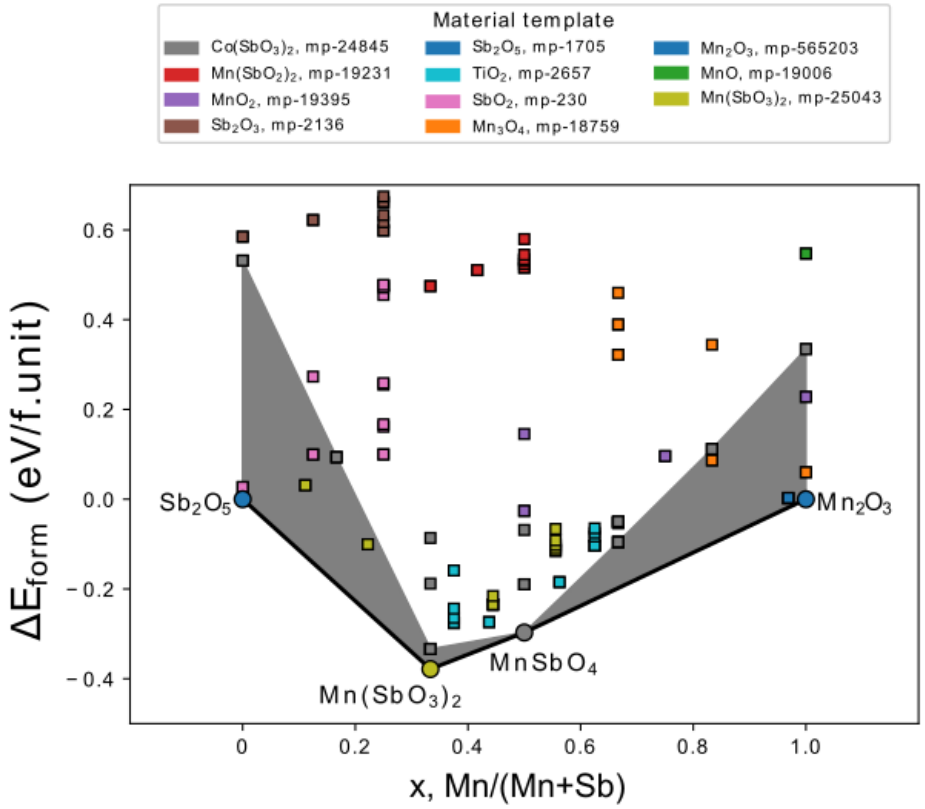

Figure S21. Grand potential phase diagram: calculated formation energy (ΔE_{form}) variation with the composition for phases in Mn-Sb-O system at 700 °C and 0.2 atm O_2, in addition to the rutile structure TiO_2 and tri-rutile $CoSb_2O_6$. The shaded grey region indicates the above hull energy of the rutile structures.

Evaluation of oxygen vacancies in Mn-rich rutile alloys

To further assess the stability of these compounds, the formation energy of defective structures were determined using DFT simulations of the most stable rutile structure at each composition with every symmetrically distinct oxygen atom removed. In Figure S22, we overlay these formation energies on the grand-potential phase diagram, which illustrates that bulk formation energies of rutile structures with oxygen vacancies are higher than those of the defect-free structure at every composition. This suggests that vacancy formation is generally unfavorable under synthesis conditions. For nearly all of the tested compositions, vacancy formation is also unfavorable relative to the most stable rutile polymorph in the Mn-Sb-O system.

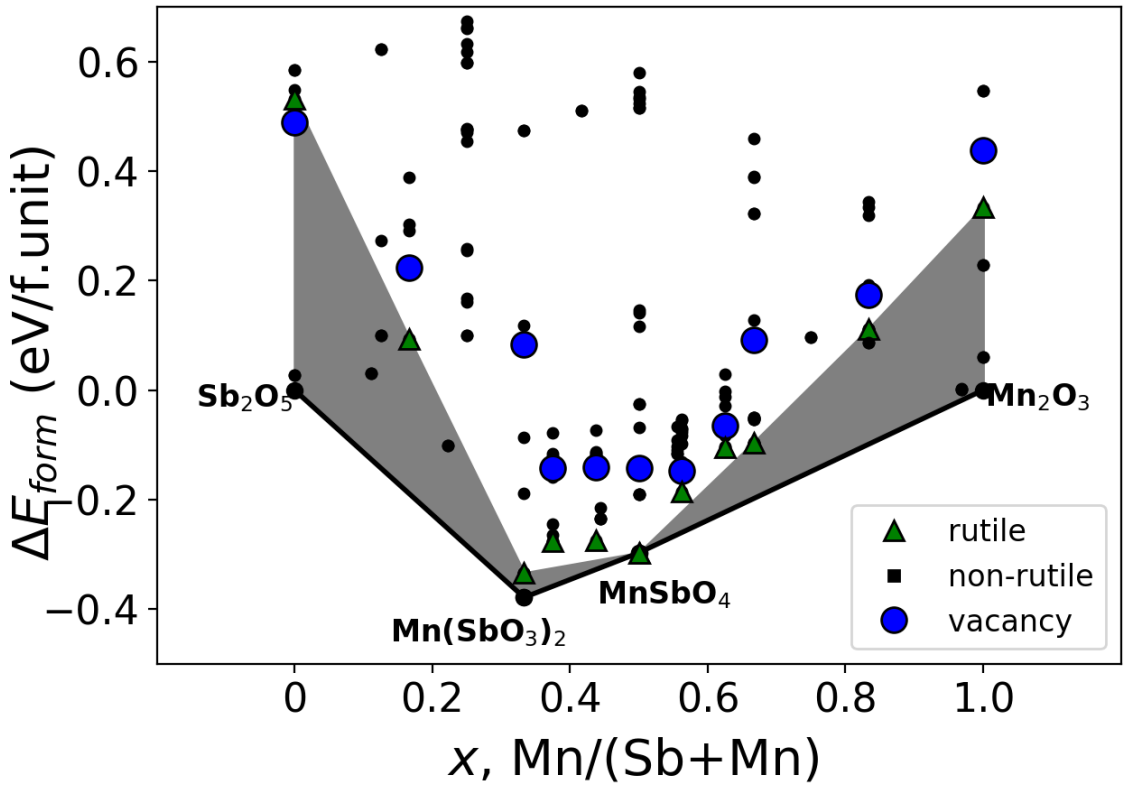

Figure S22. Grand potential phase diagram with included vacancies: the grand potential formation energy of each tested compound with additional defective structures including single oxygen vacancies. The most stable rutile structures are marked with green triangles, while the defective rutile structures are marked with blue circles.

In addition, we examine the stability of these defective structures under electrochemical conditions by plotting the Pourbaix stability of the most stable defective structure at a Sb fraction of 0.5 (Figure S23). Similar to the synthesis diagram, this demonstrates that bulk vacancies are unstable by a margin of greater than 0.3 eV over the stable region of $MnSbO_4$, and similarly as unstable as the defect-free structure outside of the Pourbaix-stable region.

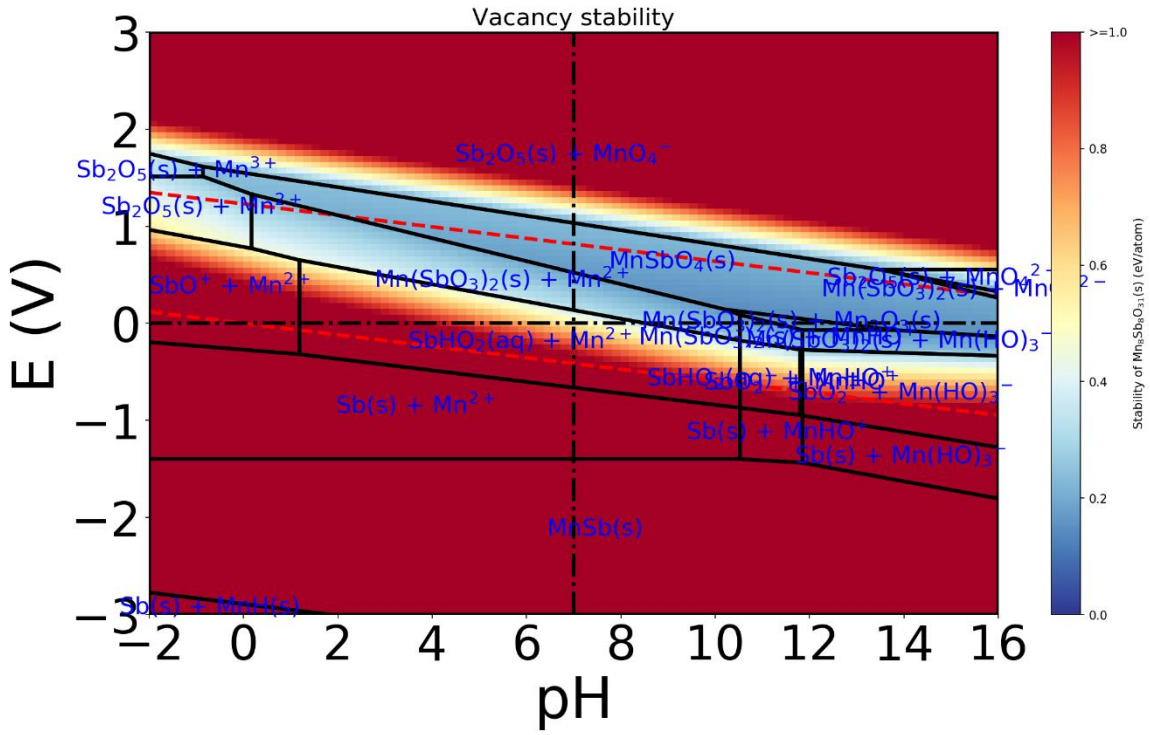

Figure S23. Pourbaix stability of structure with oxygen vacancy: the Pourbaix energy map (ΔG_{pbx}) of the most stable defective structure including one oxygen vacancy at Mn fraction of 0.5.

Calculation of number of O_2 produced per corroded metal:

Using the Pourbaix diagram of Figure 6c, the Mn corrosion mechanisms, normalized to corrosion of a single Mn, are:

- at ~1.4 V: Mn_2SbO_6 -> $MnSbO_4 + Mn^{+2} + 2\ e^- + O_2$ (2 e^- per corroded Mn)
- at ~1.6 V: $Mn_2SbO_6 + 2\ H_2O$ -> $MnSbO_4 + MnO_4^- + 3\ e^- + 4\ H^+$ (3 e^- per corroded Mn)
- >1.6 V: $0.5\ Mn_2SbO_6 + 1.5\ H_2O$ -> $0.25\ Sb_2O_5 + MnO_4^- + 2\ e^- + 3\ H^+$ (2 e^- per corroded Mn)

Since the 3 e^- reaction occurs at only a narrow voltage window, and as shown in Figure S24 no corrosion is expected at 1.4-1.6 V when the Mn concentration is 10^{-6} M, we assume 2 e^- per Mn for the calculations in Table 1. While the Pourbaix analysis diagram predicts no corrosion of Sb, for the purposes of the calculation we assume a 1 e^- reaction:

$0.5\ Sb_2O_5$ -> $SbO^+ + 0.75\ O_2 + 1\ e^-$

Using these reactions, the charge that can be attributed to Mn and Sb corrosion is determined and subtracted from the total charge passed in the electrochemical experiments, with the remainder of charge assigned to the OER. Using 4 e^- per O_2, the amount of O_2 is calculated along with the ratio of O_2 generated to corroded metal, for each metal separately.

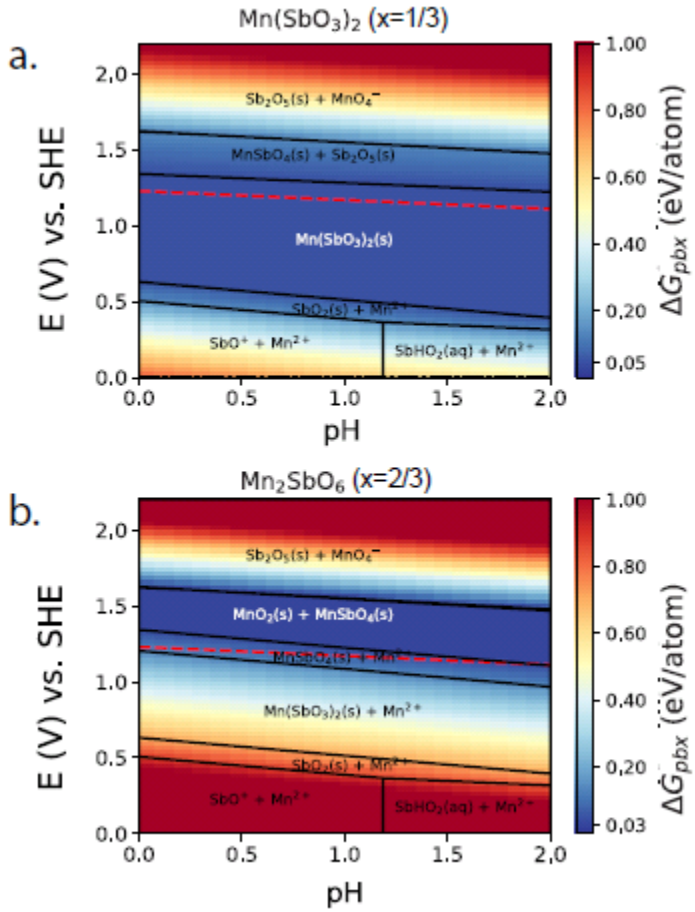

Figure S24. Computationally predicted Pourbaix diagram of Sb-Mn-O system with Mn and Sb ion concentrations each fixed at 10^{-6} M at pH = 0 - 2 range for Mn content (a) x = 1/3 and (b) x = 2/3. The Gibbs free energy (ΔG_{pbx}) of the rutile $MnSb_2O_6$ and Mn_2SbO_6 with respect to the Pourbaix stable phases is superimposed on the corresponding Pourbaix diagram and represented by the color bar. The red dashed lines denote potential of 1.23 V vs RHE (OER potential).

Table S4. Comparison of the published OER activity of non-noble metal electrocatalysts in acidic media.

Catalysts	**Overpotential (mV at 10 mA cm^{-2})**	**Substrate**	**Electrolyte (pH)**	**Stability**	**Ref.**
Mn-rich rutile $Mn_xSb_{1-x}O_z$	580	Pt/Ti/SiO_2/Si wafer	1.0 M H_2SO_4 (0)	~30 hrs electrochemistry, overpotential ~586 mV	This work
F doped $Cu_{1.5}Mn_{1.5}O_4$ nanoparticles*	320@9.15mA cm^{-2}	porous Ti foil	0.5 M H_2SO_4	24 hrs @ 16 mA cm^{-2}	[7]
C-coated Co_3O_4 nanoarray	370	Carbon paper	0.5 M H_2SO_4	86.8 hrs @100 mA cm^{-2}	[8]
Mesoporous Ag-doped Co_3O_4 nanowire arrays	370	FTO	0.5 M H_2SO_4	10 hrs @ 10 mA cm^{-2}	[9]
Ag-Co_3O_4	470	Glassy carbon	0.5 M H_2SO_4	Overpotential increased by 15-30 mV after 1000 cycles of CV	[10]
Amorphous NiFeP	540		0.05 M H_2SO_4	30 hrs @ 10 mA cm^{-2}	[11]
Crystalline Co_3O_4	570	FTO	0.5 M H_2SO_4 (0.3)	12 hrs @ 10 mA cm^{-2}	[12]
Ti-MnO_2		a gold-coated quartz crystal	0.05 M H_2SO_4 (1)	-	[13]
Co-based steel	574		0.05 M H_2SO_4 (1)	~14 hrs @ 10 mA cm^{-2}	[14]
$Ni_{0.5}Mn_{0.5}Sb_{1.7}O_y$	672 ± 9	ATO/quartz	1.0 M H_2SO_4 (0)	735 mV after 168 hrs @ 10 mA cm^{-2}	[2]

* This result has been questioned, for details see Ref.[14-15]

References

1. McCrory, C. C. L.; Jung, S.; Ferrer, I. M.; Chatman, S. M.; Peters, J. C.; Jaramillo, T. F., Benchmarking Hydrogen Evolving Reaction and Oxygen Evolving Reaction Electrocatalysts for Solar Water Splitting Devices. *J. Am. Chem. Soc.* **2015,** *137* (13), 4347-4357.
2. Moreno-Hernandez, I. A.; MacFarland, C. A.; Read, C. G.; Papadantonakis, K. M.; Brunschwig, B. S.; Lewis, N. S., Crystalline nickel manganese antimonate as a stable water-oxidation catalyst in aqueous 1.0 M H_2SO_4. *Energy Environ. Sci.* **2017,** *10* (10), 2103-2108.
3. (a) Westin, G.; Grins, J., Rutile-Type $Mn_{(1-x)}Sb_{(1+x)}O_4$ Phases, 0<=x<=1/3, Synthesized by the Sol-Gel Technique. *Acta Chem. Scand.* **1993,** *47*, 1053-1056; (b) Westin, G.; Nygren, M., Sol-Gel Preparation of M-Sb oxides from $Sb(OBu^n)_3$-M-Acetate Precursors with M=Mn, Co, Ni. *J. Mater. Chem* **1993,** *3* (4), 367-371.
4. Ravel, B.; Newville, M., ATHENA, ARTEMIS, HEPHAESTUS: data analysis for X-ray absorption spectroscopy using IFEFFIT. *J. Synchrotron Radiat.* **2005,** *12* (4), 537-541.
5. Manceau, A.; Marcus, M. A.; Grangeon, S., Determination of Mn valence states in mixed-valent manganates by XANES spectroscopy. *Am. Mineral.* **2012,** *97* (5-6), 816-827.
6. Zabinsky, S. I.; Rehr, J. J.; Ankudinov, A.; Albers, R. C.; Eller, M. J., Multiple-scattering calculations of x-ray-absorption spectra. *Phys. Rev. B* **1995,** *52* (4), 2995-3009.

7. Patel, P. P.; Datta, M. K.; Velikokhatnyi, O. I.; Kuruba, R.; Damodaran, K.; Jampani, P.; Gattu, B.; Shanthi, P. M.; Damle, S. S.; Kumta, P. N., Noble metal-free bifunctional oxygen evolution and oxygen reduction acidic media electro-catalysts. *Sci. Rep.* **2016,** *6*, 28367.
8. Yang, X.; Li, H.; Lu, A.-Y.; Min, S.; Idriss, Z.; Hedhili, M. N.; Huang, K.-W.; Idriss, H.; Li, L.-J., Highly acid-durable carbon coated Co_3O_4 nanoarrays as efficient oxygen evolution electrocatalysts. *Nano Energy* **2016,** *25*, 42-50.
9. Yan, K.-L.; Chi, J.-Q.; Xie, J.-Y.; Dong, B.; Liu, Z.-Z.; Gao, W.-K.; Lin, J.-H.; Chai, Y.-M.; Liu, C.-G., Mesoporous Ag-doped Co_3O_4 nanowire arrays supported on FTO as efficient electrocatalysts for oxygen evolution reaction in acidic media. *Renewable Energy* **2018,** *119*, 54-61.
10. Yan, K.-L.; Qin, J.-F.; Lin, J.-H.; Dong, B.; Chi, J.-Q.; Liu, Z.-Z.; Dai, F.-N.; Chai, Y.-M.; Liu, C.-G., Probing the active sites of Co_3O_4 for the acidic oxygen evolution reaction by modulating the Co^{2+}/Co^{3+} ratio. *J. Mater. Chem. A* **2018,** *6* (14), 5678-5686.
11. Hu, F.; Zhu, S.; Chen, S.; Li, Y.; Ma, L.; Wu, T.; Zhang, Y.; Wang, C.; Liu, C.; Yang, X.; Song, L.; Yang, X.; Xiong, Y., Amorphous Metallic NiFeP: A Conductive Bulk Material Achieving High Activity for Oxygen Evolution Reaction in Both Alkaline and Acidic Media. *Adv. Mater.* **2017,** *29* (32), 1606570.
12. Mondschein, J. S.; Callejas, J. F.; Read, C. G.; Chen, J. Y. C.; Holder, C. F.; Badding, C. K.; Schaak, R. E., Crystalline Cobalt Oxide Films for Sustained Electrocatalytic Oxygen Evolution under Strongly Acidic Conditions. *Chem. Mater.* **2017,** *29* (3), 950-957.
13. Frydendal, R.; Paoli, E. A.; Chorkendorff, I.; Rossmeisl, J.; Stephens, I. E. L., Toward an Active and Stable Catalyst for Oxygen Evolution in Acidic Media: Ti-Stabilized MnO_2. *Adv. Energy Mater.* **2015,** *5* (22), 1500991.
14. Schafer, H.; Kupper, K.; Muller-Buschbaum, K.; Daum, D.; Steinhart, M.; Wollschlager, J.; Krupp, U.; Schmidt, M.; Han, W.; Stangl, J., Electro-oxidation of a cobalt based steel in LiOH: a non-noble metal based electro-catalyst suitable for durable water-splitting in an acidic milieu. *Nanoscale* **2017,** *9* (45), 17829-17838.
15. Schafer, H.; Kupper, K.; Schmidt, M.; Muller-Buschbaum, K.; Stangl, J.; Daum, D.; Steinhart, M.; Schulz-Kolbel, C.; Han, W.; Wollschlager, J.; Krupp, U.; Hou, P.; Liu, X., Steel-based electrocatalysts for efficient and durable oxygen evolution in acidic media. *Catal. Sci. Technol.* **2018,** *8* (8), 2104-2116.